Microstructure dynamics in orthorhombic perovskites

Zhiying Zhang,[1] Johannes Koppensteiner,[2] Wilfried Schranz,[2] Jonathan B. Betts,[3] Albert Migliori,[3] and Michael A. Carpenter[1]

[1]*Department of Earth Sciences, University of Cambridge, Downing Street, Cambridge CB2 3EQ, United Kingdom*
[2]*Physics of Functional Materials, Faculty of Physics, University of Vienna, Strudlhofgasse 4, A-1090 Wien, Austria*
[3]*National High Magnetic Field Laboratory, Los Alamos National Laboratory, Los Alamos, New Mexico 87545, USA*

Anelastic loss mechanisms associated with phase transitions in $BaCeO_3$ have been investigated at relatively high frequency $\sim$1 MHz and low stress by resonant ultrasound spectroscopy (RUS), and at relatively low frequency $\sim$1 Hz and high stress by dynamic mechanical analysis (DMA). Changes in the elastic moduli and dissipation behavior clearly indicate phase transitions due to octahedral tilting: $Pnma \leftrightarrow Imma \leftrightarrow R\bar{3}c \leftrightarrow Pm\bar{3}m$ structures at 551 K, 670 K, and 1168 K, and strain analysis shows that they are tricritical, first-order, and second-order phase transitions, respectively. Structures with intermediate tilt states ($R\bar{3}c$ and $Imma$ structures) show substantial anelastic softening and dissipation associated with the mobility of twin walls under applied stress. The $Pnma$ structure shows elastic stiffening which may be due to the simultaneous operation of two discrete order parameters with different symmetries. In contrast with studies of other perovskites, $BaCeO_3$ shows strong dissipation at both DMA and RUS frequencies in the stability field of the $Pnma$ structure. This is evidence that ferroelastic twin walls might become mobile in $Pnma$ perovskites and suggests that shearing of the octahedra may be a significant factor.

I. INTRODUCTION

The properties and dynamics of twin walls in perovskites have been the focus of intense interest because of their unique and quite specific character as defects in otherwise homogeneous materials and because of their central role in ferroelectric, ferromagnetic, and ferroelastic switching. For example, twin walls in tungsten oxide can be induced to become superconducting while the matrix material is not,[1] and twin walls in $CaTiO_3$ might be ferrielectric in a matrix which contains no electric dipoles.[2] For the particular case of ferroelastic twin walls, the local structural changes are dominated by large strain gradients. In a perfect crystal their mobility might be expected to be unconstrained but in real crystals they experience viscous drag due to strong interaction with strain fields around defects. At low temperatures the pinning effect of defects can become sufficiently strong so that the walls become immobile. Dynamics and structure are thus closely related and can give rise to substantial variations in elastic and anelastic behaviors under the influence of an externally applied stress. Against this broader background it has been found that mechanical spectroscopy is an ideal tool for investigating twin wall properties in materials as disparate as piezoelectrics (e.g., lead-zirconate-titanate)[3–7] and analog phases for silicate perovskites $CaSiO_3$ and $(Mg,Fe)SiO_3$ in the deep earth [e.g., $LaAlO_3$ and $(Ca,Sr)TiO_3$].[8–13]

The work presented here arose from a particular conundrum in relation to the anelastic properties of perovskites with the $Pnma$ structure, as apposed to $R\bar{3}c$ or $I4/mcm$ structures. All three are improper ferroelastics containing transformation twins but the twin walls appear to be mobile only in the rhombohedral and tetragonal phases of $LaAlO_3$, $(Ca,Sr)TiO_3$, and $Sr(Zr,Ti)O_3$.[8–16] In $Ca_{1-x}Sr_xTiO_3$ with x =0.4, 0.45, and 0.5, and in $SrZrO_3$, transitions to the $Pnma$ structure are marked by a steep decrease in anelastic softening and dissipation as if twin wall motion is abruptly

curtailed.[9,14,15] Two different explanations have been offered. Daraktchiev *et al.*[14] suggested that the sign of the volume strain accompanying the transition from the parent cubic phase is important in influencing the twin wall thicknesses and hence in the extent to which they interact with defects. Alternatively, the small total spontaneous strain of $Pnma$ phases is important such that even if the walls are mobile, the strain released is small.[9,17] A more general explanation could be that the properties of twin walls in materials which have undergone structural phase transitions involving two order parameters with quite different symmetries are fundamentally different from the properties of twin walls depending on relaxations of only a single order parameter. In the case of octahedral tilting transitions, the $Pnma$ structure has nonzero order parameters belonging to irreps M_3^+ and R_4^+ while the order parameter for $R\bar{3}c$ and $I4/mcm$ belongs to R_4^+ alone. In order to distinguish between these different possibilities the mechanical behavior of other perovskites have been investigated and, quite unexpectedly, it was found that the $Pnma$ phase of $BaCeO_3$ shows strong anelastic dissipation down to $\sim$200 K. This has all the characteristics of being related to twin wall motion and provides evidence that twin walls associated with multiple order parameters in $Pnma$ perovskites might become mobile under mechanical stress.

Phase transitions in $BaCeO_3$ at ambient pressure and changing temperature follow the sequence $Pnma \leftrightarrow Imma \leftrightarrow R\bar{3}c \leftrightarrow Pm\bar{3}m$ and have previously been studied by Raman spectroscopy, neutron diffraction, x-ray diffraction (XRD), and thermal analysis.[18–23] Transition temperatures from the literature are summarized in Table I. In this study, anelastic loss mechanisms associated with the transitions were investigated at relatively high frequency $\sim$1 MHz and low stress by resonant ultrasound spectroscopy (RUS) and at relatively low frequency $\sim$1 Hz and high stress by dynamic mechanical analysis (DMA). The specific objectives were,

TABLE I. Transition temperatures for BaCeO$_3$ from previous studies. T_1 ($Pnma \leftrightarrow Imma$), T_2 ($Imma \leftrightarrow R\bar{3}c$), and T_3 ($R\bar{3}c \leftrightarrow Pm\bar{3}m$).

Method	T_1 (K)	T_2 (K)	T_3 (K)
Raman spectroscopy (Ref. 18)			1073
Neutron diffraction (Ref. 19)	563	673	1173
Neutron diffraction (Ref. 20)	573	673	1200
Raman spectroscopy (Ref. 20)	533	700	1153
Thermal analysis (Ref. 21)	530 ± 10	665 ± 10	1170 ± 20
Thermal analysis (Ref. 22)	540	600	1180
Thermal analysis (Ref. 23)	533	658	1168
X-ray diffraction (Ref. 23)	553	673	1173
RUS[a]	551	670	1168
DMA[a]	551	670	
Strain analysis[a]	530	673	1170 ± 2

[a]This study.

first, to compare the $Pnma \leftrightarrow Imma \leftrightarrow R\bar{3}c \leftrightarrow Pm\bar{3}m$ sequence of BaCeO$_3$ with the comparable but subtly different $Pnma \leftrightarrow Imma \leftrightarrow I4/mcm \leftrightarrow Pm\bar{3}m$ sequence of SrZrO$_3$, second, to examine the anelastic behavior of the $Imma$ structure which appears as an intermediate phase in some perovskites but not in others, third, to characterize the anelastic loss behavior of the $Pnma$ structure and, finally, to correlate the overall elastic behavior with details of the spontaneous strain evolution extracted from high-resolution lattice-parameter data.

II. STRAIN ANALYSIS OF SUCCESSIVE PHASE TRANSITIONS

Lattice parameters obtained by Knight[19] from high-resolution powder neutron diffraction have been used to follow the evolution of individual order parameters, in terms of symmetry-adapted spontaneous strains, through the sequence of phase transitions in BaCeO$_3$. The original data are reproduced in Figs. 1(a) and 1(b) for the reduced pseudocubic unit cell, with the orthorhombic values in the $Pnma$ setting used by Knight.[24] Values of the cubic reference parameter a_o were obtained by fitting a straight line to data at temperatures between 1198 and 1273 K in the stability field of the $Pm\bar{3}m$ structure, giving $a_o = 4.3384 + 0.000046T$ with T in kelvins [Fig. 1(a)]. The volume strain and tetragonal shear strain are defined as

$$e_a = e_1 + e_2 + e_3, \tag{1}$$

$$e_{tx} = \frac{1}{\sqrt{3}}(2e_1 - e_2 - e_3), \tag{2}$$

and the remaining nonzero shear strain is e_4. The orientations of unit-cell axes with respect to the reference system for the strain tensor are the same as given by Carpenter *et al.*[25–27] Expressions for the individual strains in terms of the unit-cell dimensions of $Pnma$, $Imma$, and $R\bar{3}c$ structures are listed in Table II. Variations in the spontaneous strains calculated on this basis are shown in Fig. 1(c). Note that shear strains are insensitive to the choice of a_o but uncertainties in a_o result in significant uncertainties in the absolute values of e_a.

Octahedral tilting transitions in perovskites can be described by order parameters which are associated with M and R points of the Brillouin zone of the cubic parent structure and have symmetry properties of irreps M_3^+ and R_4^+, respectively.[25,28,29] The two order parameters each contain three components. A complete Landau expansion, to sixth order in the order parameters and including coupling with the strains, has been given by Carpenter.[29] M-point order-parameter components are q_1, q_2, and q_3, R-point components are q_4, q_5, and q_6: the $R\bar{3}c$ structure has $q_4 = q_5 = q_6 \neq 0$ and $q_1 = q_2 = q_3 = 0$, the $Imma$ structure has $q_4 = q_6 \neq 0$ and $q_1 = q_2 = q_3 = q_5 = 0$, and the $Pnma$ structure has $q_4 = q_6 \neq 0$, $q_2 \neq 0$, and $q_1 = q_3 = q_5 = 0$. Relationships between these order-parameter components and the spontaneous strains[15,25,26,30]
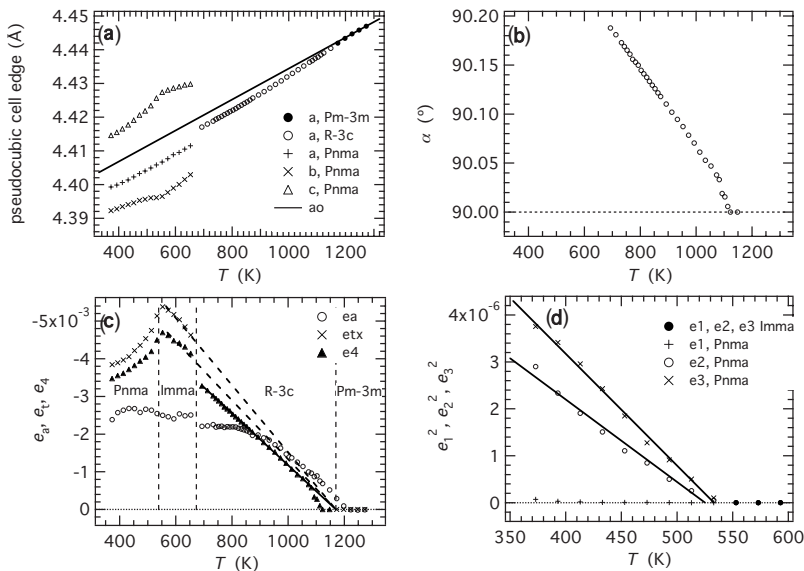

FIG. 1. [(a) and (b)] Lattice parameter data (Ref. 19) given in terms of the pseudocubic unit cell. The straight line in (a) represents the reference lattice parameter, a_o, obtained by fitting to data in the temperature interval 1198–1273 K. (c) Symmetry-adapted strains, with respect to the parent $Pm\bar{3}m$ structure, derived from the lattice parameters in (a) and (b). A straight line fit to data for e_4 of the $R\bar{3}c$ structure in the temperature interval 693–1083 K extrapolates to zero at $T_c = 1170 \pm 2$ K. Broken lines are fits to e_4 and e_{tx} of the $Imma$ structure constrained to have $T_c = 1170$ K. (d) Variations in linear strains of the $Pnma$ structure defined with respect to the $Imma$ structure as reference state. In this case e_2^2 and e_3^2 vary approximately linearly with temperature, implying close to tricritical character for the $Imma \leftrightarrow Pnma$ transition, with $T_c \approx 530$ K.

TABLE II. Relationships between spontaneous strains and order-parameter components of $R\bar{3}c$, $Imma$, and $Pnma$ structures, with respect to the cubic $Pm\bar{3}m$ parent structure derived from Eq. (1) of Ref. 29 (see also Refs. 27 and 36). Orientation relationships between crystallographic axes and the reference axes are illustrated in Refs. 25 and 26.

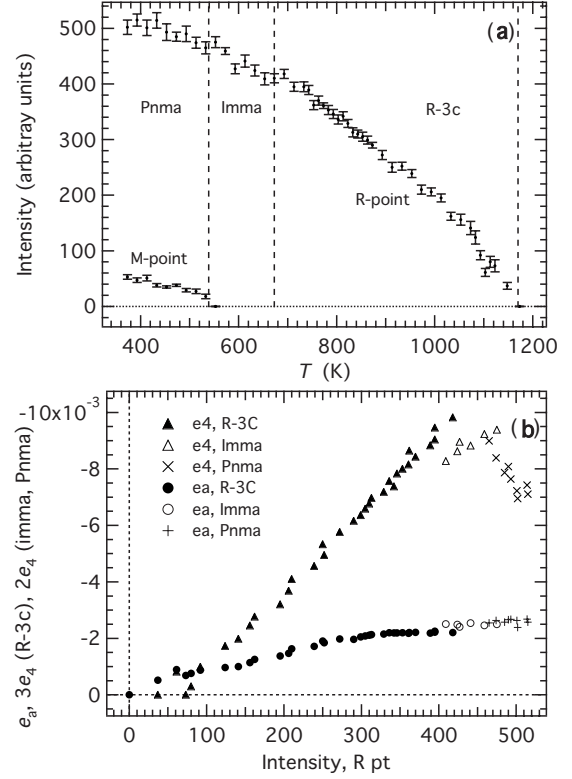| $R\bar{3}c$	$Imma$	$Pnma$
$e_a = -\dfrac{3\lambda_2 q_4^2}{\frac{1}{3}(C_{11}^o + 2C_{12}^o)}$	$e_a = -\dfrac{2\lambda_2 q_4^2}{\frac{1}{3}(C_{11}^o + 2C_{12}^o)}$	$e_a = -\dfrac{(\lambda_1 q_2^2 + 2\lambda_2 q_4^2)}{\frac{1}{3}(C_{11}^o + 2C_{12}^o)}$
$e_{ox} = 0$	$e_{ox} = 0$	$e_{ox} = 0$
$e_{tx} = 0$	$e_{tx} = \dfrac{2\lambda_4 q_4^2}{\frac{1}{2}(C_{11}^o - C_{12}^o)}$	$e_{tx} = -\dfrac{2(\lambda_3 q_2^2 - \lambda_4 q_4^2)}{\frac{1}{2}(C_{11}^o - C_{12}^o)}$
$e_4 = e_5 = e_6 = -\dfrac{\lambda_5 q_4^2}{C_{44}^o}$	$e_4 = -\dfrac{\lambda_5 q_4^2}{C_{44}^o}$	$e_4 = -\dfrac{(\lambda_5 q_4^2 + \lambda_{eM2+M3} + q_2 q_{2JT})}{C_{44}^o}$
	$e_5 = e_6 = 0$	$e_5 = e_6 = 0$
$e_1 = e_2 = e_3 = \dfrac{\frac{a}{2} - a_o}{a_o}$	$e_1 = \dfrac{\frac{b}{2} - a_o}{a_o}$	$e_1 = \dfrac{\frac{b}{2} - a_o}{a_o}$
	$e_2 + e_3 = \dfrac{\frac{a}{\sqrt{2}} - a_o}{a_o} + \dfrac{\frac{c}{\sqrt{2}} - a_o}{a_o}$	$e_2 + e_3 = \dfrac{\frac{a}{\sqrt{2}} - a_o}{a_o} + \dfrac{\frac{c}{\sqrt{2}} - a_o}{a_o}$
$e_4 = -\dfrac{a}{a_o}\cos\alpha$	$e_4 = \dfrac{\frac{a}{\sqrt{2}} - a_o}{a_o} - \dfrac{\frac{c}{\sqrt{2}} - a_o}{a_o}$	$e_4 = \dfrac{\frac{a}{\sqrt{2}} - a_o}{a_o} - \dfrac{\frac{c}{\sqrt{2}} - a_o}{a_o}$

FIG. 2. (a) Intensities of R-point and M-point superlattice reflections, reproduced from Ref. 24. (b) Relationships between symmetry-adapted strains and R-point superlattice reflection intensities. For e_a, data relating to all three superstructure types fall on the same trend, implying that the coupling coefficient between the volume strain and the order parameter is constant. For e_4 there is a small break between data for the $R\bar{3}c$ and $Imma$ structures, implying that coupling between e_4 and the order parameter is slightly weaker in the $Imma$ structure than in the $R\bar{3}c$ structure. Data for e_4 of the $Pnma$ structure fall off the trend due to the influence of an additional order-parameter component.

are listed in Table II, with C_{ik}^o representing elastic constants of the $Pm\bar{3}m$ reference structure in the usual way. In the $R\bar{3}c$ structure, e_4 is expected to scale with q_4^2 and the data are consistent with $e_4 \propto q_4^2 \propto T$ [Fig. 1(c)].[24] The $Pm\bar{3}m \leftrightarrow R\bar{3}c$ transition is therefore second order in character and the straight line fit to data for the temperature interval 693–1083 K gave $T_c = 1170 \pm 2$ K. Data for the temperature interval 1093–1148 K fall below the linear trend but at such small values the deviations from cubic geometry are at or below the limits of resolution of the primary diffraction data.

The $R\bar{3}c \leftrightarrow Imma$ transition is marked by small discontinuities in e_a and e_4 [Fig. 1(c)] and is first order in character.[19,24] In principle, there is a metastable $Pm\bar{3}m \leftrightarrow Imma$ transition with the same critical temperature as for the $Pm\bar{3}m \leftrightarrow R\bar{3}c$ transition. Limited data for e_{tx} and e_4 of the $Imma$ phase (both $\propto q_4^2$) can at least be interpreted on this basis [Fig. 1(c)]. As in the case of the $Pm\bar{3}m \leftrightarrow I4/mcm \leftrightarrow Imma \leftrightarrow Pnma$ sequence in SrZrO$_3$ (Ref. 15) and the $Pm\bar{3}m \leftrightarrow I4/mcm \leftrightarrow Pnma$ sequence in CaTiO$_3$,[25] e_a does not scale linearly with the shear strains, suggesting higher order coupling effects or a temperature-dependent order-parameter coupling coefficient for the volume strain.

Lattice parameter data show continuous variations through the $Imma \leftrightarrow Pnma$ transition [Fig. 1(a)] and these convert to continuous variations in the magnitudes of both e_4

and e_{tx} [Fig. 1(c)], though with nonlinear dependences on temperature. If the reference state for this transition is taken as the $Imma$ structure, the transition will have a single order parameter, Q, and the linear strains are expected to scale as $e_1 \propto e_2 \propto e_3 \propto Q^2$. Using straight line fits to the data for a, b, and c of the $Imma$ structure to obtain a_o, b_o, and c_o, the linear strains $e_1 = (a - a_o)/a_o$, $e_2 = (b - b_o)/b_o$, and $e_3 = (c - c_o)/c_o$ (reference axes $X \| \boldsymbol{a}$, $Y \| \boldsymbol{b}$, and $Z \| \boldsymbol{c}$) have been determined and these scale with temperature approximately as $e_1^2 \propto e_2^2 \propto e_3^2 \propto Q^4 \propto T$ [Fig. 1(d)]. The transition is thus close to tricritical, with $T_c \approx 530$ K.

Intensity data for M- and R-point superlattice reflections are reproduced from Ref. 24 in Fig. 2(a). They show a continuous decrease to zero at ~540 K and ~1170 K, respectively, together with a small discontinuity at ~673 K. Intensities of the R-point reflections, I_R, are expected to be proportional to Q^2, where Q is the scalar order parameter and $|Q| = \sqrt{3q_4^2}$ for the $R\bar{3}c$ structure, or $|Q| = \sqrt{2q_4^2}$ for the $Imma$ structure. For the $R\bar{3}c$ structure, $e_4 \propto I_R$ is observed [Fig. 2(b)], though a straight line through the data does not pass through the origin (probably as a consequence of Debye-

Waller contributions or because the background intensity was not accounted for quite correctly). The e_4 data have been plotted in Fig. 2(b) as $3e_4$ and $2e_4$, respectively, for the $R\bar{3}c$ and *Imma* structures (since $e_4 = -\lambda_5 q_4^2 / C_{44}^o$ in each case) to test whether the discontinuity is due entirely to the discontinuity in Q or whether there is also a change in the strength of the coupling coefficient, λ_5. The fact that the *Imma* values plot slightly below the $R\bar{3}c$ values implies that λ_5 reduces slightly in the *Imma* structure. On the other hand, data for e_a follow the same trend for both structures, implying that λ_2 remains the same. Thus the $R\bar{3}c \leftrightarrow Imma$ transition is marked by a small reduction in both the R-point order parameter and in the strength of coupling with e_4.

The tetragonal shear strain e_{tx} decreases at the *Imma* $\leftrightarrow$ *Pnma* transition due to the influence of M-point tilting (Table II). On the other hand, e_4 couples with the M-point order parameter only as $(\lambda_6 + \lambda_7)e_4^2 q_2^2$ and this coupling influences the strain evolution as (from Refs. 15 and 29)

$$e_4 = -\frac{\lambda_5 q_4^2}{C_{44}^o + 2(\lambda_6 + \lambda_7)q_2^2}. \tag{3}$$

It is generally assumed that C_{44}^o is much greater than $(\lambda_6 + \lambda_7)q_4^2$ so that the additional term in the denominator can be dropped. In this case, e_4 should continue to increase with I_R in the stability field of the *Pnma* structure but it actually decreases [Figs. 1(c) and 2(b)]. This can be explained by the operation of an additional, secondary, order parameter of the *Pnma* structure. From a symmetry analysis of cooperative Jahn-Teller transitions in perovskites two types of ordering of distorted octahedra were identified by Carpenter and Howard.[27] These are associated with irreps Γ_3^+ and M_2^+ of the parent cubic space group and correspond to ordering of the unique axis of uniaxially distorted octahedra parallel to the crystallographic b axis or ordered in a staggered arrangement within planes parallel to (010). The Γ_3^+ order parameter couples biquadratically with e_4 and therefore would be expected to contribute to e_4 only in the same manner as q_2 in Eq. (3). On the other hand, the M_2^+ order parameter (components $q_{1JT} = q_{3JT} = 0$ and $q_{2JT} \neq 0$ under *Pnma* symmetry) has a coupling term of the form $\lambda_{eM2+M3+}e_4 q_2 q_{2JT}$ so that the variation in e_4 becomes (from Ref. 27)

$$e_4 = \frac{-\lambda_5 q_4^2 - \lambda_{eM2+M3+}q_2 q_{2JT}}{C_{44}^o}. \tag{4}$$

If q_{2JT} varies approximately linearly with q_2, the observed pattern of nonlinear variation in e_4 for a tricritical transition would result. In other words, the strain evolution can be understood in terms of the normal effects of octahedral tilting together with a significant contribution from deformation of individual octahedra which mimics the larger distortions that occur at cooperative Jahn-Teller transitions in perovskites with the *Pnma* structure, as described by Carpenter and Howard.[27,31]

In summary, the magnitudes of the strains are generally typical of those accompanying octahedral tilting transitions in perovskites. Formal strain analysis confirms second-order

character for the $Pm\bar{3}m \leftrightarrow R\bar{3}c$ transition, first-order character for the $R\bar{3}c \leftrightarrow Imma$ transition, and approximately tricritical character for the *Imma* $\leftrightarrow$ *Pnma* transition. The $R\bar{3}c \leftrightarrow Imma$ transition is accompanied by a small reduction in the amount of R-point tilting and a small reduction in the strength of coupling with the shear strain e_4. The data do not provide evidence of whether the strength of coupling between R-point order-parameter components and e_{tx} (coupling coefficient λ_4) differs between the $R\bar{3}c$, *Imma*, and *Pnma* structures. The *Imma* $\leftrightarrow$ *Pnma* transition gives rise to a reduction in the magnitude of both e_{tx} and e_4, indicating that strain-mediated coupling between the M-point and R-point tilts is unfavorable. Evidence of the nonlinear dependence of the volume strain e_a and the contribution of an M_2^+ component to e_4 implies that the overall transition mechanism involves some degree of deformation of the CeO_6 octahedra. As well as having opposite sign, the pattern of variation in e_4 in the *Pnma* structure of $BaCeO_3$ differs from that shown by $CaTiO_3$ (Ref. 25) and $SrZrO_3$.[15] Finally, e_a is negative in $CaTiO_3$ (Ref. 25) and $BaCeO_3$ (this analysis) and positive at most temperatures in $SrZrO_3$.[15]

III. ELASTICITY: EXPERIMENTAL DETAILS

$BaCeO_3$ powder, used by Knight[19,24] for neutron-diffraction experiments, was ground in acetone using an agate ball mill at 600 rpm for 1 h with PULVERISETTE 7 from FRITSCH. The milled powder, $\sim$5 g, was pressed into a cylindrical pellet of diameter 13 mm and height $\sim$6 mm using a pellet die under $\sim$1800 psi for 5 min with an Omega Bench Press from SHINN FU. The pellet was sintered in air at 1450 °C for 48 h and the detailed procedure is as follows. (1) Heated from 20 to 1400 °C at 10 °C/min. (2) Held at 1400 °C for 2 h. (3) Heated from 1400 to 1450 °C at 5 °C/min. (4) Held at 1450 °C for 48 h. (5) Cooled from 1450 to 20 °C at 3 °C/min.

Rectangular parallelepiped samples were cut from the sintered pellet using an annular diamond saw, lubricated with paraffin. The parallelepiped used for RUS measurements had dimensions $1.66 \times 2.11 \times 2.64$ mm^3 and mass 0.053 g. The density determined from these parameters is 5.73 g/cm^3, which is $\sim$91% of the theoretical density, 6.29 g/cm^3.[32] For DMA tests, a sample was polished to the dimensions $\sim$0.22 $\times$ 2.00 $\times$ 7.20 mm^3. An offcut of the sample was also crushed and investigated by XRD, using a Bruker D8 diffractometer with Cu K_α radiation at 40 kV and 40 mA. The diffraction angle 2θ was scanned from 5° to 95°. Steps were in increments of 0.02° and the counts were collected for 3 s at each step. The diffraction pattern was entirely consistent with the known orthorhombic structure of $BaCeO_3$.

RUS data were collected at low temperatures (10–300 K) using dynamic resonance system modulus II electronics, and an orange helium flow cryostat, as described by McKnight *et al.*[33] Frequency was scanned from 100 to 1200 kHz. High-temperature data (300–1300 K) for the same frequency range were collected using alumina buffer rods protruding into a horizontal Netzsch furnace[34] and Stanford electronics described by Migliori and Maynard.[35] The elastic moduli were
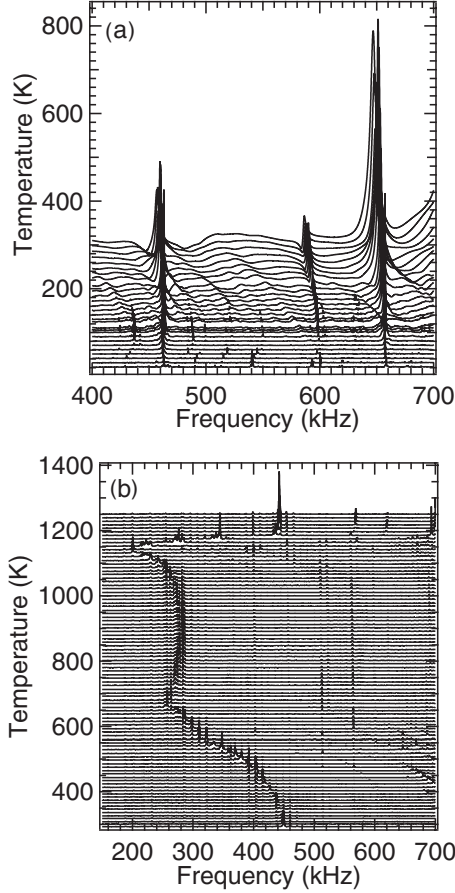
FIG. 3. Stacks of RUS scans. (a) Low temperatures: the weak background peaks at very low temperatures are noise from somewhere in the sample holder. (b) High temperatures: the regularly spaced background peaks are due to alumina rods.

determined from fitting 27 resonance peaks with an overall root-mean-square error of ~0.3%. In addition, internal friction, i.e., inverse of quality factor Q was obtained from asymmetric Lorentz fitting of the resonance peak, $Q^{-1} = \Delta f / f_0$. Δf is full width at half maximum of the resonance peak, and f_0 is the resonance frequency. Temperature measured by a thermocouple close to the sample was calibrated using Eq. (5), determined from known transition temperatures of single-crystal quartz (846 K), LaAlO$_3$ (817 K), and Ca$_{0.7}$Sr$_{0.3}$TiO$_3$ (1204 K), as described by McKnight *et al.* (Ref. 15),

$$T_{\text{cal.}} = 4.3766 + 0.98604 \times T_{\text{read}}. \tag{5}$$

DMA tests were performed using a diamond DMA from PerkinElmer within the temperature range 150–800 K. The sample was mounted on knife edges in three-point bending geometry. Static and dynamic forces $F_s + F_d \exp(i\omega t)$ are applied in the frequency range of 0.1–100 Hz using a steel rod. There is a phase lag δ between the applied force and the sample's deflection response, which is read out via the displacement of the rod u_{d}. Attenuation $\tan \delta$, storage modulus E' (real component of complex Young's modulus), and loss modulus E'' (imaginary component of complex Young's modulus) were determined,
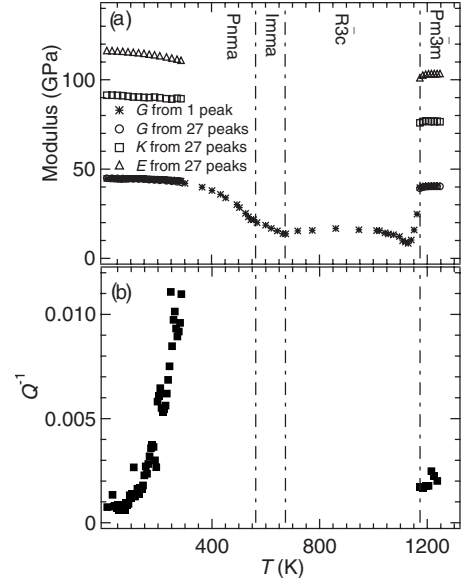

FIG. 4. Temperature dependencies of elastic moduli and inverse quality factor Q^{-1} determined by RUS.

$$\tan \delta = E''/E', \tag{6}$$

$$E = E' + iE'' = \frac{l^3}{4t^3 w} \frac{F_D}{u_D} \exp(i\delta). \tag{7}$$

l is the spacing between the two bottom knife edges, 5.00 mm; t is the thickness of the sample, ~0.22 mm; and w is the width of the sample, ~2.00 mm. $F_s = 60$ mN, $F_D = 50$ mN, gain 1, amplitude 5 μm, and maximum deformation 100 μm were used for all measurements. The sample was heated from room temperature to 800 K and then cooled back to room temperature. Next, the sample was cooled to 150 K and then heated back to room temperature. The heating and cooling rates were all at 3 °C/min.

IV. ELASTICITY RESULTS

The elastic moduli determined by RUS at room temperature are as follows. The bulk modulus K of BaCeO$_3$ is 88.9 GPa, the shear modulus G is 42.4 GPa, the longitudinal modulus L is 145.4 GPa, Young's modulus E is 109.6 GPa, and Poisson's ratio ν is 0.294. Stacks of RUS scans at low and high temperatures are shown in Figs. 3(a) and 3(b), respectively. In general, the resonance frequencies decrease with increasing temperature. There are clear anomalies in the general trend at 551 K, 670 K, 1130 K and 1168 K, respectively. These correspond closely to the *Pnma* $\leftrightarrow Imma \leftrightarrow R\bar{3}c \leftrightarrow Pm\bar{3}m$ transitions determined from the strain analysis given above, with the exception of the frequency minimum at ~1130 K, which occurs ~40 K below the $R\bar{3}c \leftrightarrow Pm\bar{3}m$ transition point. The transition temperatures are consistent with the reports in literature, which are summarized in Table I. The temperature dependencies of shear modulus G, bulk modulus K, and Young's modulus E are illustrated in Fig. 4(a). At temperatures below 298 K and
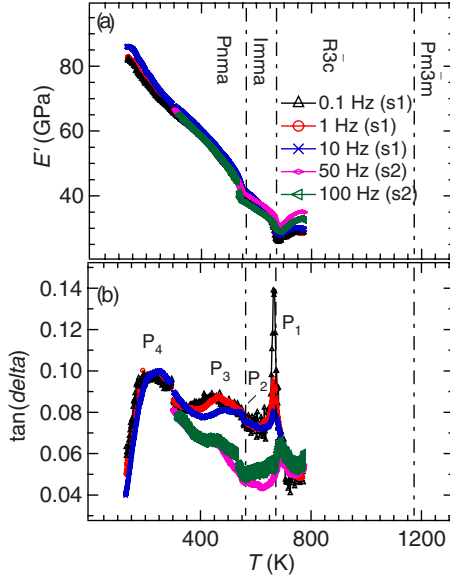
FIG. 5. (Color online) Temperature dependencies of storage modulus E' and dissipation $\tan\delta$ measured at different frequencies by DMA during cooling. Static force=60 mN, dynamic force =50 mN, gain=1, amplitude=5 μm, maximum deformation =100 μm, and cooling rate=3 °C/min. s1 and s2 represent different samples.

above 1180 K, the resonance peaks were strong and values of the elastic parameters are from fitting. Between 298 and 1180 K, most of the resonance peaks were too weak to be detected but the variation in shear modulus over the entire temperature range could still be determined from the frequencies of the first resonance peak. This is essentially due to a pure shear mode and its frequency was calibrated using

$$G_{\mathrm{T}} = \frac{f_{\mathrm{T}}^2 G_{298}}{f_{298}^2}, \tag{8}$$

where f_{298} and G_{298} are, respectively, the frequency of the first peak and the fitted value of G at 298 K. Good agreement is obtained with data obtained from peak fitting at lower temperatures. In general, the elastic moduli decrease with increasing temperature up to the cubic↔rhombohedral transition. Stability limits for the different phases from diffraction data have been added to Fig. 4 to show that anomalies correspond to the known transition temperatures. Figure 4(b) shows the temperature dependence of Q^{-1} determined by RUS at temperatures where individual resonance peaks were well resolved and distinct from regularly spaced background peaks due to the alumina rods. Dissipation in the *Pnma* phase increases with increasing temperature and is not measureable above ~0.011 at ~290 K. Dissipation is then relatively low in the $Pm\bar{3}m$ stability field.

Figure 5(a) shows the temperature dependence of the storage modulus determined by DMA. It is consistent with the result obtained by RUS as shown in Fig. 4(a). Note, of course, that RUS gives the shear modulus while the storage modulus in DMA relates to Young's modulus. In general, the storage modulus decreases with increasing temperature. The
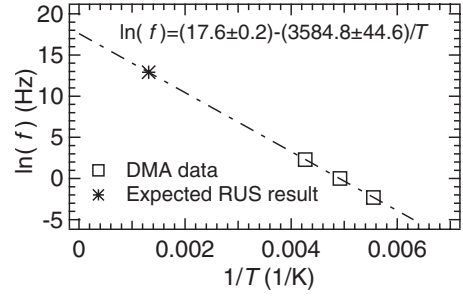

FIG. 6. $\ln(f)$ vs $1/T$ with frequency and temperature determined for maxima in dissipation of peak P_4. The fitting gives activation energy $E_{\mathrm{a}}=29.8\pm0.4$ kJ/mol and $f_0=44.4$ MHz.

changes in slope indicate phase transitions. Kinks are shown at the transitions $Pnma \leftrightarrow Imma$ at ~551 K and $Imma \leftrightarrow R\bar{3}c$ at ~670 K, respectively. With increasing frequency, the storage modulus increases slightly and the transition temperatures remain the same. The temperature dependencies of the dissipation measured at different frequencies are shown in Fig. 5(b). There are a few distinct peaks, labeled P_1–P_4 from high temperature to low temperature. The sharp peak P_1 at ~670 K clearly relates directly to the first-order $Imma \leftrightarrow R\bar{3}c$ transition. It has a sharp maximum, which reduces in magnitude but does not shift in temperature with increasing frequency. Peak P_2 at ~551 K is small and clearly relates to the $Pnma \leftrightarrow Imma$ transition. It does not obviously vary with frequency. Peaks P_3 and P_4 are broad and occur at ~460 K and ~200 K, respectively, within the stability field of the *Pnma* structure. With increasing frequency, both peaks shift to higher temperatures implying that they are related to thermally activated dissipation processes. The activation energy E_{a} has been determined from the frequencies and temperatures for peak P_4 using the temperature of maximum in Q^{-1},

$$\ln f = \ln f_0 - \frac{E_{\mathrm{a}}}{RT}. \tag{9}$$

This gives $E_{\mathrm{a}}=29.8\pm0.4$ kJ/mol and $f_0=44.4$ MHz (Fig. 6). Peak P_3 is not reproducible in heating and cooling (Fig. 7), and therefore has not been fitted in the same way.

V. DISCUSSION

RUS and DMA data show clear patterns of changes in the elastic moduli and dissipation behavior of $BaCeO_3$ due to octahedral tilting transitions. In particular, close agreement has been found between the temperatures of each anomaly in the elastic properties and the transition temperatures obtained from lattice-parameter variations and other measurements. As found in previous RUS (Refs. 12, 15, and 16) and DMA studies,[8,9,14] structures with intermediate tilt states ($I4/mcm$, $R\bar{3}c$, and *Imma*) have significantly smaller values of shear modulus than the cubic $Pm\bar{3}m$ and the orthorhombic *Pnma* structures. In contrast with studies of other perovskites, however, $BaCeO_3$ shows strong dissipation at both DMA and RUS frequencies in the stability field of the *Pnma* structure.
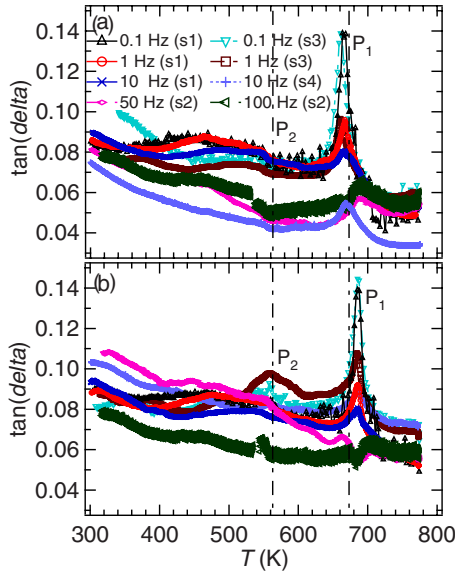
FIG. 7. (Color online) Temperature dependence of dissipation tan δ measured at different frequencies by DMA. (a) During heating. (b) During cooling. Static force=60 mN, dynamic force =50 mN, gain=1, amplitude=5 μm, maximum deformation =100 μm, heating rate=3 °C/min, and cooling rate=3 °C/min. s1, s2, s3, and s4 represent different samples. The data appear to include multiple overlapping peaks through the temperature interval ~350–600 K, and it has not been possible to extract an activation energy from them.

The origins of these similarities and differences are considered here in terms of strain effects and through comparison with previously reported behavior of $LaAlO_3$, $(Ca,Sr)TiO_3$, $Sr(Zr,Ti)O_3$, and $(Sr,Ba)SnO_3$.

A. Elastic softening

The pattern of anomalies in the shear modulus observed at RUS frequencies for the transformation sequence $Pnma \leftrightarrow Imma \leftrightarrow R\bar{3}c \leftrightarrow Pm\bar{3}m$ in $BaCeO_3$ is essentially the same as for the $Pnma \leftrightarrow Imma \leftrightarrow I4/mcm \leftrightarrow Pm\bar{3}m$ sequence in $SrZrO_3$ reported by McKnight et al.[15] During cooling the first transition from the parent cubic structure is marked by a steep softening. In the case of a second-order transition, the standard Landau solution would be for a reduction in elastic constants which is independent of temperature. Similar patterns have been seen for other compositions across the $Sr(Zr,Ti)O_3$ solid solution.[16] In the case of the $R\bar{3}c \leftrightarrow Pm\bar{3}m$ transition in $LaAlO_3$, additional softening in the rhombohedral phase through an interval of ~100 K below T_c is due to coupling of acoustic modes with a central peak mode.[36] The same mechanism is likely to account for the nonlinear softening of $BaCeO_3$ as the transition is approached from below T_c [Fig. 4(a)].

On the basis of a standard Landau model, the first-order transitions $Imma \leftrightarrow R\bar{3}c$ in $BaCeO_3$ and $Imma \leftrightarrow I4/mcm$ in $SrZrO_3$, would be expected to be marked simply by a small discontinuity in elastic constants. Instead, some softening is observed as the transition temperature is approached from

both sides and this has been attributed to a degree of local fluctuations between different tilt orientations.[15] In both materials the $Pnma \leftrightarrow Imma$ transition is close to tricritical in character, with a break in slope of the shear modulus and marked stiffening in the $Pnma$ phase. Similar stiffening is seen as a function of composition in $(Ca,Sr)TiO_3$.[37] Elastic stiffening, rather than softening at an improper ferroelastic transition implies that the usual mechanism of order-parameter relaxation due to some applied stress does not operate. The pattern of stiffening observed in $SrAl_2O_4$ by Carpenter et al.[38] was also not consistent with this mechanism and the feature in common between these two completely different structures is the existence of two separate order parameters belonging to different irreducible representations. The physical origin of this change in behavior is not understood and it remains to be seen whether it is a universal phenomenon.

The pattern of elastic softening (and acoustic dissipation) observed at DMA frequencies for $BaCeO_3$ is also closely similar to that reported for the sequence $Pnma \leftrightarrow Imma \leftrightarrow I4/mcm \leftrightarrow Pm\bar{3}m$ in $Sr_xBa_{1-x}SnO_3$ by Daraktchiev et al.[14] On the basis of transition temperatures given in Daraktchiev et al.,[39] the composition appears to be $x=0.9$ rather than $x=0.8$ as given (see, also, discussion in Ref. 15).

B. Anelastic dissipation

The Peak P_1 in Fig. 5(b) shows that tan δ increases with decreasing measurement frequency, f. Assuming a relaxation process with relaxation time τ, dissipation is expected to follow tan $\delta \propto \frac{\omega\tau}{1+\omega^2\tau^2}$, where $\omega=2\pi f$. To obtain the observed increase in tan δ with decreasing frequency one then would have to assume $\omega\tau>1$ even at 0.1 Hz, leading to $\tau>1.6$ s. There are at least two possible origins for such a slow dynamics. First, heat diffusion could lead to such a low-frequency dynamics as in $KMnF_3$.[40] However, a calculation of the corresponding relaxation time (Ref. 41) $\tau_{th} \approx \frac{t^2}{\pi^2 D_{th}}$, where $t=0.022$ cm is the sample thickness and D_{th} =0.004 cm²/s (Ref. 22), gives $\tau_{th}=0.012$ s which is far too short in comparison with the estimated value of $\tau=1.6$ s. Moreover an evaluation of the Pippard relations using the thermal expansivity $\alpha \approx 10^{-5}$ K^{-1} (Ref. 42) yields a difference of the adiabatic and isothermal elastic constants $C^S - C^T \approx 0.1$ GPa at T_2. Therefore an isothermal adiabatic crossover due to heat diffusion can be ruled out for a possible origin of the P_1 peak.

The second possibility for low-frequency dispersion of the P_1 peak in $BaCeO_3$ could be phase front motion due to the first-order nature of the phase transition. Internal friction peaks associated with the movement of interfaces between coexisting phases at a first-order transition have been measured in a number of systems including $BaTiO_3$,[43,44] Fe-Mn alloy,[45] and CuAlBe alloy.[46] These internal friction peaks have in common that the peak height increases with decreasing frequency and is independent of the measuring strain amplitude. Zhang et al.[47] have calculated the dissipation function resulting from the movement of first-order-induced interfaces, yielding
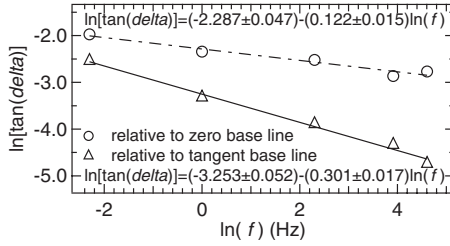
FIG. 8. Double logarithmic plot $\ln(\tan \delta)$ vs $\ln(f)$ for maxima in dissipation of peak P_1. Two fitting processes were used to determine values of $\tan \delta$. The first was for no baseline correction (zero baseline). The second used a baseline tangential to data points at ~600 and ~750 K. The decay is consistent with power law $\tan \delta = Af^n$, where $-0.301 < n < -0.122$.

$$Q^{-1} = A(T)\left(\frac{\dot{T}}{\omega}\right)^{n_1} + B(T)\omega^{-n_2}, \quad (10)$$

where $\dot{T}$ is the heating/cooling rate, and $A(T)$ and $B(T)$ are temperature-dependent coefficients. Since $\tan \delta \approx Q^{-1}$ (Ref. 48) the theoretical analysis of the frequency dependence of the loss angle in the transition regime leads to the power-law dependence of Eq. (10). A double-logarithmic plot of the frequency dependence of the height of the loss peak is consistent with power law $\tan \delta = Af^n$, where n is between -0.301 and -0.122 (Fig. 8). The value of the exponent n is very similar to the value -0.2 in Ref. 46.

The small P_2 peak is independent of frequency but, in marked contrast with $Ca_{0.5}Sr_{0.5}TiO_3$ and $Sr_xBa_{1-x}SnO_3$,[14] is followed by a temperature interval of high $\tan \delta$ rather than a steep reduction in anelastic loss. Peak P_3 does not appear to be reproducible between samples whereas peak P_4 seems to be a well-defined Debye peak for a thermally activated dissipation process. Overall the evolution of $\tan \delta$ in the *Pnma* field of $BaCeO_3$ is similar to that observed in the $R\bar{3}c$ field of $LaAlO_3$,[49] and in the $I4/mcm$ field of $Ca_{0.3}Sr_{0.7}TiO_3$,[9] except that the Debye peak is shifted down from ~410 to ~250 K and the activation energy is reduced from ~80–100 to ~30 kJ/mol. Harrison *et al.*[11] were able to determine by direct observation of twin wall motion that the Debye peak in $LaAlO_3$ is due to a freezing process whereby the walls become effectively pinned by defects. The defects are believed to be oxygen vacancies. By analogy it is proposed here that the loss behavior in $BaCeO_3$ is also due to mobile transformation twin walls, making this the first perovskite in which the *Pnma* structure has twin walls which are potentially mobile on a time scale of seconds. If the loss at DMA frequencies and applied stresses is due to twin wall motion, Fig. 6 implies that freezing at 400 kHz would be at 760 K. Substantial dissipation occurs well below this temperature at RUS frequencies, however, suggesting that a slightly different twin wall related loss mechanism operates under conditions of low stress as in the case of $LaAlO_3$.[13]

C. Strain behavior

Elastic anomalies are characteristically related to strain anomalies so that similarities and differences in the elastic behavior of $BaCeO_3$ relative to other perovskites should also be reflected in the spontaneous strains accompanying each of the phase transitions. In terms of Landau parameters, the principal difference between $SrZrO_3$ and $BaCeO_3$ is the value of one of the two fourth-order coefficients for the R_4^+ order parameter, as renormalized by coupling with shear strains. Equation (11) includes two such coefficients and leads to the constraint $b'^* > 0$ for $R\bar{3}c$ stability and $b'^* < 0$ for $I4/mcm$ stability,[36] where

$$b'^* = b' + \frac{\lambda_3^2}{C_{44}^o} - \frac{12\lambda_2^2}{\frac{1}{2}(C_{11}^o - C_{12}^o)}. \quad (11)$$

The coefficients λ_3 and λ_2 describe the strength of coupling between the order parameter and rhombohedral and tetragonal/orthorhombic strains, respectively. The change in transition sequences can be understood simply in terms of the relative strengths of these two couplings but it is not clear how this difference, by itself, could be responsible for different anelastic properties of the *Pnma* structure.

Daraktchiev *et al.*[14] drew attention to the sign of the volume strain as a potentially important factor. $LaAlO_3$ and $Sr_{0.2}Ba_{0.8}SnO_3$ both have positive volume strains associated with the cubic to rhombohedral or tetragonal transition while $CaTiO_3$ and $Ca_{0.6}Sr_{0.4}TiO_3$ have negative volume strains. They postulated that this would result in relatively thick twin walls in the former and relatively thin walls in the latter and, hence, in different strengths of interaction with defects. In $SrZrO_3$ the volume strain is negative over a small temperature interval and then positive but shows no dissipation in the *Pnma* stability field.[15] $BaCeO_3$ has a negative volume strain [Fig. 2(c)] and apparently mobile twin walls, so there is no systematic correlation.

Data given in Refs. 15 and 25 and Fig. 2 show that the tetragonal shear strain e_{tx} has a similar evolution in $SrZrO_3$, $CaTiO_3$, and $BaCeO_3$, making this an unlikely factor in the context of different dynamic behavior for *Pnma* twin walls. On the other hand, $SrZrO_3$ and $CaTiO_3$ both have positive e_4 strains with anomalous dependence on tilt angles while $BaCeO_3$ has a negative e_4 strain which follows the M_3^+ and R_4^+ tilts exactly as would be expected on the basis of the lowest-order coupling terms [Fig. 2(c)]. Equation (4) shows that the second tilt system, M_3^+, contributes to e_4 only via distortions of the perovskite octahedra. Regular distortions which scale with the M_3^+ tilt apparently occur in $BaCeO_3$ while some other style of shearing of the octahedra would be required to produce the e_4 shear strain shown by $SrZrO_3$. If there is a significant difference in structural distortions of the bulk material, it follows that there will also be differences in the structure of the twin walls. Either there is then some additional geometrical constraint to twin wall motion arising from an alternative style of octahedral shearing or the twin wall thicknesses change. As discussed in detail by Lee *et al.*[50] and qualitatively by Daraktchiev *et al.*,[14] thick walls are expected to interact less strongly with defects than thin walls and, in the event that the width of the walls becomes greater than the effective dimension of the defect, the interaction will tend to zero. For $BaCeO_3$ there is dissipation in the

Pnma structure which also extends to lower temperatures than the similar dissipation in other $R\bar{3}c$ and $I4/mcm$ perovskites and the activation energy for freezing is lower. Both geometrical constraints and different interaction with defects therefore seem to be implicated if the loss behavior is related directly to twin walls.

VI. CONCLUSIONS

Perovskites with only one tilt system operating show substantial anelastic softening and dissipation associated with the mobility of twin walls under applied stress. The *Imma* phase of $BaCeO_3$, at least, shows slightly higher dissipation than the $R\bar{3}c$ phase but the overall pattern of softening is consistent with that expected on the basis of strain/order parameter relaxations. All *Pnma* phases so far examined show elastic stiffening which is counter to the expectation from standard Landau coupling models, and the simultaneous operation of two discrete order parameters with different symmetries appears to be the common factor in this behavior. Distinctive anelastic behavior of the *Pnma* structure of $BaCeO_3$ correlates with a difference in the shear strain e_4, and this appears to implicate shearing of the octahedra as an important factor in either providing some additional geometrical constraints on wall mobility or in causing weaker interaction with defects (or both). This provides an additional variable which can be manipulated by choice of perovskite composition in the wider context of tailoring the structure and properties of twin walls in materials used for switching or other device applications. For example, it will be interesting to find whether the twin walls in *Pnma* $BaCeO_3$ are ferrielectric, as appears to be case for the same twin walls in $CaTiO_3$.[2] Finally, the prospect is now raised that the *Pnma* structure of $(Mg,Fe)SiO_3$ perovskite in the deep earth might contain mobile twin walls and, hence, cause attenuation of seismic waves. The key factor for analysis of this possibility will be the nature of any octahedral shearing which accompanies tilting at extreme pressure and temperature.

[1] A. Aird and E. K. H. Salje, J. Phys.: Condens. Matter **10**, L377 (1998).

[2] L. Goncalves-Ferreira, S. A. T. Redfern, E. Artacho, and E. K. H. Salje, Phys. Rev. Lett. **101**, 097602 (2008).

[3] V. S. Postnikov, V. S. Pavlov, and S. K. Turkov, J. Phys. Chem. Solids **31**, 1785 (1970).

[4] C. Wang, Q. F. Fang, Y. Shi, and Z. G. Zhu, Mater. Res. Bull. **36**, 2657 (2001).

[5] C. Wang, Q. F. Fang, and Z. G. Zhu, Appl. Phys. Lett. **80**, 3578 (2002).

[6] C. Wang, S. A. T. Redfern, M. Daraktchiev, and R. J. Harrison, Appl. Phys. Lett. **89**, 152906 (2006).

[7] E. M. Bourim, H. Tanaka, M. Gabbay, G. Fantozzi, and B. L. Cheng, J. Appl. Phys. **91**, 6662 (2002).

[8] R. J. Harrison and S. A. T. Redfern, Phys. Earth Planet. Inter. **134**, 253 (2002).

[9] R. J. Harrison, S. A. T. Redfern, and J. Street, Am. Mineral. **88**, 574 (2003).

[10] R. J. Harrison, S. A. T. Redfern, and U. Bismayer, Miner. Mag. **68**, 839 (2004).

[11] R. J. Harrison, S. A. T. Redfern, and E. K. H. Salje, Phys. Rev. B **69**, 144101 (2004).

[12] J. N. Walsh, P. A. Taylor, A. Buckley, T. W. Darling, J. Schreuer, and M. A. Carpenter, Phys. Earth Planet. Inter. **167**, 110 (2008).

[13] M. A. Carpenter, A. Buckley, P. A. Taylor, and T. W. Darling, J. Phys.: Condens. Matter **22**, 035405 (2010).

[14] M. Daraktchiev, R. J. Harrison, E. H. Mountstevens, and S. A. T. Redfern, Mater. Sci. Eng., A **442**, 199 (2006).

[15] R. E. A. McKnight, C. J. Howard, and M. A. Carpenter, J. Phys.: Condens. Matter **21**, 015901 (2009).

[16] R. E. A. McKnight, B. J. Kennedy, Q. Zhou, and M. A. Carpenter, J. Phys.: Condens. Matter **21**, 015902 (2009).

[17] M. A. Carpenter, Am. Mineral. **92**, 328 (2007).

[18] T. Scherban, R. Villeneuve, L. Abello, and G. Lucazeau, Solid State Commun. **84**, 341 (1992).

[19] K. S. Knight, Solid State Ionics **74**, 109 (1994).

[20] F. Genet, S. Loridant, C. Ritter, and G. Lucazeau, J. Phys. Chem. Solids **60**, 2009 (1999).

[21] A. V. Kuzmin, V. P. Gorelov, B. T. Melekh, M. Glerup, and F. W. Poulsen, Solid State Ionics **162-163**, 13 (2003).

[22] S. Yamanaka, T. Hamaguchi, T. Oyama, T. Matsuda, S. Kobayashi, and K. Kurosaki, J. Alloys Compd. **359**, 1 (2003).

[23] T. Ohzeki, S. Hasegawa, M. Shimizu, and T. Hashimoto, Solid State Ionics **180**, 1034 (2009).

[24] K. S. Knight, Solid State Ionics **145**, 275 (2001).

[25] M. A. Carpenter, A. I. Becerro, and F. Seifert, Am. Mineral. **86**, 348 (2001).

[26] M. A. Carpenter, C. J. Howard, B. J. Kennedy, and K. S. Knight, Phys. Rev. B **72**, 024118 (2005).

[27] M. A. Carpenter and C. J. Howard, Acta Crystallogr., Sect. B: Struct. Sci. **65**, 134 (2009).

[28] C. J. Howard and H. T. Stokes, Acta Crystallogr., Sect. B: Struct. Sci. **54**, 782 (1998).

[29] M. A. Carpenter, Am. Mineral. **92**, 309 (2007).

[30] M. A. Carpenter, C. J. Howard, K. S. Knight, and Z. Zhang, J. Phys.: Condens. Matter **18**, 10725 (2006).

[31] M. A. Carpenter and C. J. Howard, Acta Crystallogr., Sect. B: Struct. Sci. **65**, 147 (2009).

[32] S. Loridant, L. Abello, E. Siebert, and G. Lucazeau, Solid State Ionics **78**, 249 (1995).

[33] R. E. A. McKnight, M. A. Carpenter, T. M. Darling, A. Buckley, and P. A. Taylor, Am. Mineral. **92**, 1665 (2007).

[34] R. E. A. McKnight, T. Moxon, A. Buckley, P. A. Taylor, T. W. Darling, and M. A. Carpenter, J. Phys.: Condens. Matter **20**, 075229 (2008).

[35] A. Migliori and J. D. Maynard, Rev. Sci. Instrum. **76**, 121301 (2005).

[36] M. A. Carpenter, S. V. Sinogeikin, and J. D. Bass, J. Phys.: Condens. Matter **22**, 035404 (2010).

[37] M. A. Carpenter, B. Li, and R. C. Liebermann, Am. Mineral. **92**, 344 (2007).

[38] M. A. Carpenter, A. Buckley, P. A. Taylor, R. E. A. McKnight, and T. W. Darling, J. Phys.: Condens. Matter **22**, 035406 (2010).

[39] M. Daraktchiev, E. K. H. Salje, W. T. Lee, and S. A. T. Redfern, Phys. Rev. B **75**, 134102 (2007).

[40] W. Schranz, A. Tröster, A. V. Kityk, P. Sondergeld, and E. K. H. Salje, Europhys. Lett. **62**, 512 (2003).

[41] A. Tröster and W. Schranz, Phys. Rev. B **66**, 184110 (2002).

[42] S. Yamaguchi and N. Yamada, Solid State Ionics **162-163**, 23 (2003).

[43] B. L. Cheng, M. Gabbay, G. Fantozzi, and W. Duffy, Jr., J. Alloys Compd. **211-212**, 352 (1994).

[44] J. X. Zhang, W. Zheng, P. C. W. Fung, and K. F. Liang, J. Alloys Compd. **211-212**, 378 (1994).

[45] P. C. W. Fung, J. X. Zhang, Y. Lin, K. F. Liang, and Z. C. Lin, Phys. Rev. B **54**, 7074 (1996).

[46] E. K. H. Salje, H. Zhang, H. Idrissi, D. Schryvers, M. A. Carpenter, X. Moya, and A. Planes, Phys. Rev. B **80**, 134114 (2009).

[47] J. X. Zhang, P. C. W. Fung, and W. G. Zeng, Phys. Rev. B **52**, 268 (1995).

[48] T. Lee, R. S. Lakes, and A. Lal, Rev. Sci. Instrum. **71**, 2855 (2000).

[49] R. J. Harrison, S. A. T. Redfern, A. Buckley, and E. K. H. Salje, J. Appl. Phys. **95**, 1706 (2004).

[50] W. T. Lee, E. K. H. Salje, L. Goncalves-Ferreira, M. Daraktchiev, and U. Bismayer, Phys. Rev. B **73**, 214110 (2006).